

OPTICS

Quantum magnetic gradiometer with entangled twin light beams

Shuhe Wu^{1,2}, Guzhi Bao^{1,2*}, Jinxian Guo^{1,2}, Jun Chen^{1,2}, Wei Du^{1,2}, Minwei Shi^{1,2}, Peiyu Yang^{1,2}, Liqing Chen^{2,3*}, Weiping Zhang^{1,2,4,5*}

In the past few decades, optical magnetometry has experienced remarkable development and reached to an outstanding sensitivity. For magnetometry based on optical readout of atomic ensemble, the fundamental limitation of sensitivity is restricted by spin projection noise and photon shot noise. Meanwhile, in practical applications, ambient magnetic noise also greatly limits the sensitivity. To achieve the best sensitivity, it is essential to find an efficacious way to eliminate the noises from different sources, simultaneously. Here, we demonstrate a quantum magnetic gradiometer with sub-shot-noise sensitivity using entangled twin beams with differential detection. The quantum enhancement spans a frequency range from 7 Hz to 6 MHz with maximum squeezing of 5.5 dB below the quantum noise limit. The sensitivity of gradiometer reaches $18 \text{ fT/cm}\sqrt{\text{Hz}}$ at 20 Hz. Our study inspires future possibilities to use quantum-enhanced technology in developing sensitive magnetometry for practical applications in noisy and physically demanding environments.

INTRODUCTION

Precision measurement technology based on optical magnetometry with high sensitivity (1–7) has great potential for applications in a diversity of fields, such as fundamental physics (8–13), biomag (14–19), chemistry (20, 21), materials science (22–26), geology (27), and astronomy (28). So far, there have existed several limits including spin projection noise (SPN), photon shot noise (PSN), and ambient magnetic field noise, which are the obstacles to further improving the sensitivity of conventional magnetometry. To reach high sensitivity in the conventional magnetometer, the SPN and PSN are usually minimized as low as possible by optimizing the atom number and photon number. Although sophisticated techniques (1–7) have been developed for this purpose, in practical applications with demanding conditions such as low operation temperature or Earth's magnetic field, these techniques have been nearly pushed to their limits. Squeezed light becomes a promising candidate to further enhance the sensitivity in this scenario (29).

Quantum-enhanced magnetometry with squeezed light has been proposed and demonstrated for decades (30–37). Because of technically existing incompatibility between squeezing source and magnetometer, the quantum enhancement has not been observed at low frequencies and the enhanced sensitivity remains subpicotesla level even at high frequencies, which greatly restricts its practicability in certain applications requiring high sensitivity at low frequencies (10–22, 25–28). On the other hand, the now reported quantum-enhanced magnetometry is well shielded from ambient magnetic field noise. In reality with noisy environment, the ambient magnetic field noise becomes dominant above the quantum noise, especially in an unshielded environment, as

shown in Fig. 1A. The quantum enhancement cannot be observed in this situation. To eliminate the influence of noisy environment, the effective way is to operate a pair of magnetometers, one of which serves as a reference sensor in a gradiometric configuration (7, 38–40). The ambient magnetic field noise coupling to the pair of magnetometers as common-mode magnetic field noise (CMMN) can be effectively canceled with a high common-mode rejection ratio (CMRR). The utilization of the reference sensor here is to monitor the ambient magnetic field noise but at the price of adding quantum noise to the gradiometer due to the totally doubled number of particles in the configuration as shown in Fig. 1B. To further improve the sensitivity in such a quantum noise only-limited gradiometer, it is desired to develop new techniques based on quantum optics to squeeze the noise below the quantum noise limit and, meanwhile, to eliminate the additional quantum noise for the gradiometer. Here, we propose and demonstrate a quantum gradiometer by combining entangled twin beams and gradiometric detection into optical magnetometry, as shown in Fig. 1C. By implementing entangled twin beams in two fully polarized atomic ensembles as probe beams to couple the magnetic field into the polarization of the beams, the PSN and additional quantum noise are suppressed by entanglement, and, meanwhile, the CMMN are removed by gradiometric detection as well. The quantum enhancement spans a frequency range from 7 Hz to 6 MHz with maximum squeezing of 5.5 dB below the quantum noise limit, and a maximum CMRR reaches 5000. As a result, the sensitivity of gradiometer reaches $18 \text{ fT/cm}\sqrt{\text{Hz}}$ at 20 Hz. This is the best sensitivity and highest enhancement achieved to date in the magnetometry with quantum light. The developed quantum gradiometer opens up new possibilities to reach high sensitivity for practical applications such as magnetoencephalography and geomagnetic sensing in noisy and physically demanding environments.

¹School of Physics and Astronomy, and Tsung-Dao Lee Institute, Shanghai Jiao Tong University, Shanghai 200240, China. ²Shanghai Branch, Hefei National Laboratory, Shanghai 201315, China. ³State Key Laboratory of Precision Spectroscopy, Quantum Institute for Light and Atom, Department of Physics, East China Normal University, Shanghai 200062, China. ⁴Shanghai Research Center for Quantum Sciences, Shanghai 2013, China. ⁵Collaborative Innovation Center of Extreme Optics, Shanxi University, Taiyuan, Shanxi 030006, China.

*Corresponding author. Email: guzhibao@sjtu.edu.cn (G.B.); lqchen@phy.ecnu.edu.cn (L.C.); wpz@sjtu.edu.cn (W.Z.)

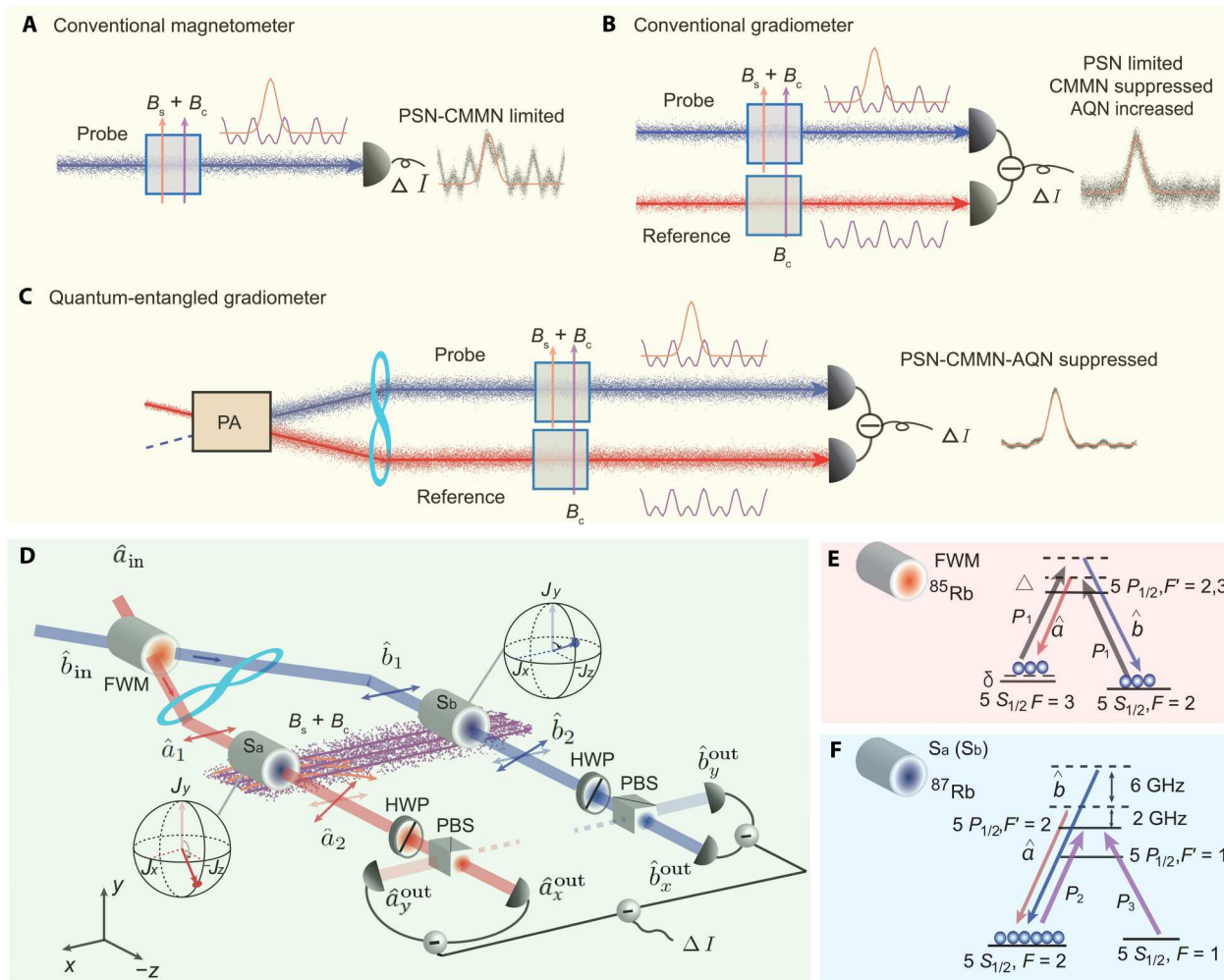


Fig. 1. The protocols and schematic diagram of quantum-entangled gradiometer. In the case of single sensor (A), the noise of conventional magnetometer is limited by both PSN and common-mode magnetic field noise (CMMN). For the conventional gradiometer (B), the measured CMMN of the two sensors is identical, while the additional quantum noise (AQN) is uncorrelated. With differential measurement, the CMMN is suppressed, while the additional quantum noise is increased because of the doubled photon number. When the entangled twin beams are used as the probe fields for the magnetic measurement (C), both noises are suppressed, while the magnetic signal remains. PA, parametric amplifier; PBS, polarization beam splitter; B_c , CMMN; B_s , magnetic signal. (D) Schematic diagram of quantum gradiometer. HWP, half-wave plate; B_L , leading magnetic field. (E and F) Energy level diagram in the D_1 line of ^{85}Rb for four-wave mixing (FWM) process and energy level diagram in the D_1 line of ^{87}Rb for optical magnetometry with modulated light. Δ , one-photon detuning; δ , two-photon detuning; P_1 , FWM pump field; P_2 , optical pumping of optical magnetometry with modulated light; P_3 , optical repumping of optical magnetometry with modulated light.

RESULTS

The quantum gradiometer consists of two parts: generation of entangled twin beams and a magnetic gradiometer. The schematic diagram is shown in Fig. 1D. Entangled twin beams \hat{a}_1 and \hat{b}_1 act as the probe beams of two atomic sensors to couple magnetic field B into their polarizations as \hat{a}_2 and \hat{b}_2 . \hat{a}_2 and \hat{b}_2 are split at the polarization beam splitter (PBS). The output fields, designated \hat{a}_x^{out} , \hat{a}_y^{out} , \hat{b}_x^{out} , and \hat{b}_y^{out} , are detected to achieve optical rotation signals. The experimental setup is shown in Fig. 2, and the details are mentioned in Materials and Methods. Below, we give the experimental operation and results. We focus on how to reduce quantum noise and eliminate CMMN at frequencies of 1 to 100 Hz in the experimental operation.

Twin beams

Entangled twin beams are generated by a four-wave mixing (FWM) process in ^{85}Rb atomic vapor (41–44), which shows the best squeezing available at the wavelength of 795 nm. A horizontally polarized pump laser of 100 mW and an orthogonally polarized signal field \hat{a}_{in} of 10 μW are combined by a Glan-Laser polarizer at an angle of 0.4° to satisfy the phase match condition and sent into an ^{85}Rb vapor cell. The generated twin beams, designated \hat{a}_1 and \hat{b}_1 , can be given as

$$\hat{a}_1 = G\hat{a}_{\text{in}} + e^{i\Phi_p}g\hat{b}_{\text{in}}^\dagger \quad (1)$$

$$\hat{b}_1 = G\hat{b}_{\text{in}} + e^{i\Phi_p}g\hat{a}_{\text{in}}^\dagger \quad (2)$$

where G and g are the gain factors satisfying $G^2 - g^2 = 1$. Φ_p is the

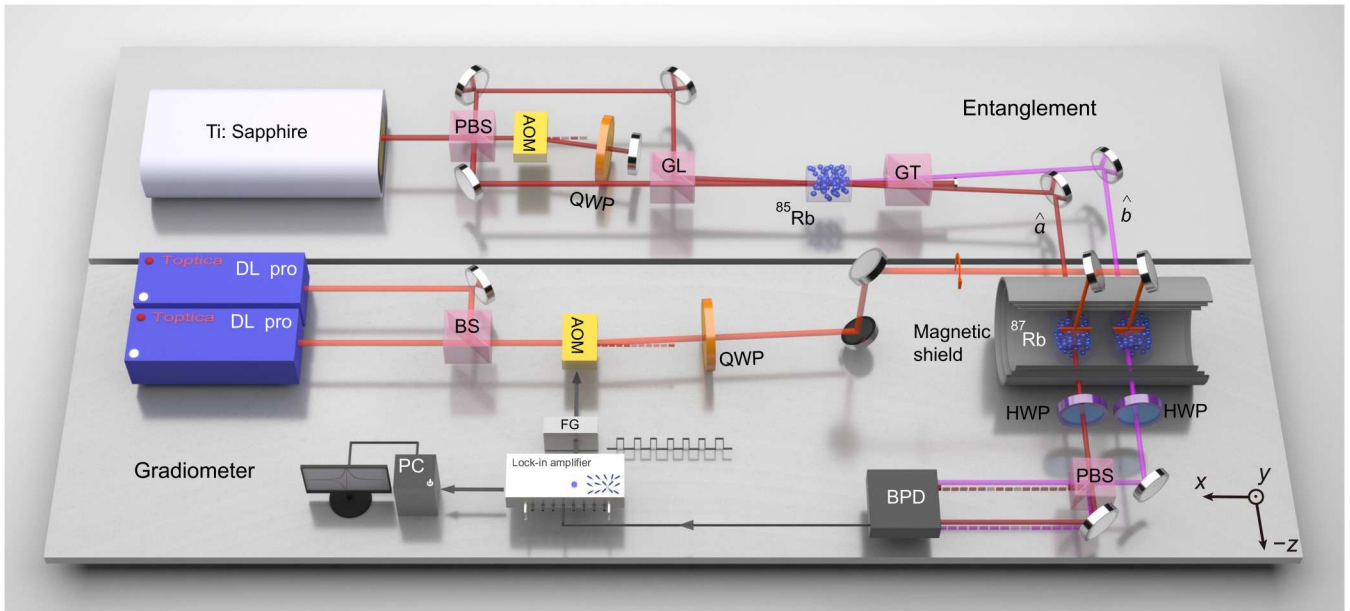


Fig. 2. Experimental setup. AOM, acousto-optic modulator; BS, 50/50 beam splitter; QWP, quarter-wave plate; FG, function generator; GL, Glan-Laser polarizer; GT, Glan-Thomson polarizer; BPD, balanced photodetector.

phase related to the pump beam. With a coherent state $|\alpha\rangle$ input at port \hat{a}_{in} and vacuum at port \hat{b}_{in} , the noise of intensity difference $\hat{a}_1^\dagger \hat{a}_1 - \hat{b}_1^\dagger \hat{b}_1$ is squeezed compared with the coherent light of the same power. The squeezing is independent of the phase Φ_p (see details in Materials and Methods). The frequency of the pump field is 1 GHz blue-detuned from the transition $|5S_{1/2}, F=2\rangle \rightarrow |5P_{1/2}, F'=2\rangle$ of ^{85}Rb atom at 795 nm. The seed \hat{a}_{in} is red-detuned approximately 3 GHz from the pump beam by using an acousto-optic modulator (AOM) in double-pass configuration. After the ^{85}Rb cell, a Glan-Thomson (GT) polarizer is used to filter out the pump beam. The generated twin beams \hat{a}_1 and \hat{b}_1 are both $\sim 150 \mu\text{W}$ in power with $G=3.9$ and horizontally polarized along the \hat{x} direction. The squeezing spans a frequency range of 6 MHz. The maximum squeezing is 7 dB at 0.6 MHz.

Quantum gradiometer

To measure the gradient magnetic field, two isotopically enriched ^{87}Rb vapor cells are used as the two sensors (S_a and S_b) of the gradiometer. The atomic spins of S_a and S_b are synchronously oriented along \hat{y} (polarized to the $|5S_{1/2}, F=2, m_F=2\rangle$ state) by two circularly polarized laser beams (P_2^a/P_3^a and P_2^b/P_3^b) with modulation frequency Ω_m (45, 46). Here, P_2^a and P_3^a are optical pumping and repumping for sensor S_a ; P_2^b and P_3^b are optical pumping and repumping for sensor S_b . The optical pumping beam is resonant with $5S_{1/2}, F=2$ to $5P_{1/2}, F'=2$ transition to polarize the atoms. The optical repumping beam is resonant with $5S_{1/2}, F=1$ to $5P_{1/2}, F'=2$ transition to pump most of the atoms to $F=2$ states. Both optical pumping and repumping beams are split and sent to the two sensors (S_a and S_b) of the gradiometer. By synchronously modulating the intensity of optical pumping and repumping beams with a square wave modulation (3% duty cycle) by AOMs, the atomic spins are periodically driven and start Larmor precession. The power of optical pumping and repumping beams

during the “on” part of the cycle is 5 mW and 30 mW, respectively. After the twin beams propagate through the atomic medium, the electric field amplitude ϵ , overall phase ϕ , polarization angle θ , and ellipticity ϵ are all modulated at Larmor frequency Ω_L (47, 48). With the existence of a leading magnetic field B_L along the \hat{x} direction, the atomic spins of S_a and S_b start to undergo Larmor precession with Larmor frequencies of Ω_L^a and Ω_L^b , respectively. The magnetic field gradient along the x direction is given as $\partial B_L/\partial x = (\Omega_L^a - \Omega_L^b)/\gamma D_{ab}$, where γ is the gyromagnetic ratio and D_{ab} is the distance between the two sensors.

Entangled twin beams \hat{a}_1 and \hat{b}_1 are sent into S_a and S_b as the probe fields for the magnetic measurement. The frequencies of \hat{a}_1 and \hat{b}_1 are approximately 3 GHz red- and blue-detuned from the pump field for ^{85}Rb vapor, i.e., approximately 2 and 8 GHz detuned from the transition $|5^2S_{1/2}, F=2\rangle \rightarrow |5^2P_{1/2}, F=2\rangle$ of the ^{87}Rb atom, respectively. The two probe beams are both far off-resonant with the ^{87}Rb atomic transition, atom-light interaction can be approximated to the first order (49)

$$\hat{H} = \beta_o \hat{S}_z^o \hat{J}_z^o \quad (o = a, b) \quad (3)$$

where β_o is the coupling constant, $\hat{S}_z^o = i(\hat{\sigma}_y^\dagger \hat{\sigma}_x - \hat{\sigma}_x^\dagger \hat{\sigma}_y)$ is the Stokes parameter, and \hat{J}_z^o is the macroscopic atomic spin along the \hat{z} axis for sensor S_o , $o = a$ and b represent S_a and S_b , respectively.

After the twin beams propagate through the atomic sensors, the polarization angles of the two beams are rotated by $\Delta\theta_a \propto \beta_a \hat{J}_z^a$ and $\theta_b \propto \beta_b \hat{J}_z^b$, which are related to the respective magnetic fields on the atomic sensors. The rotated output beams are designated \hat{a}_2 and \hat{b}_2 . Each beam is split by a PBS, converting the rotation angles into intensity modulation. The final output fields \hat{a}_x^{out} and \hat{b}_y^{out} (\hat{a}_y^{out} and \hat{b}_x^{out}) are mixed and detected by a balanced photodetector (BPD;

Thorlabs, PDB450A) with two photodiodes (S 3883) of high quantum efficiency (96%) obtaining optical rotation signal I . The fluctuation of optical rotation signal I , which denotes the noise of the quantum magnetometer, is (see details in Materials and Methods)

$$\begin{aligned} \text{Var}(I) &= [G^2 - g^2 \cos(4\theta_0)] |\alpha^2| + 2\sin^2(2\theta_0)g^2 \\ &= \text{Var}_{\text{PSN}} - 2g^2(|\alpha^2| + 1)\cos^2(2\theta_0) \end{aligned} \quad (4)$$

where α is the amplitude of the two probe beams, θ_0 is the relative angle between the optical axis of the half-wave plate (HWP) and the \hat{x} axis, and Var_{PSN} is the PSN with a power equal to the total power of the twin beams.

With the perturbations $\Delta\theta_a$ and $\Delta\theta_b$, the change in the optical rotation signal is (see details in Materials and Methods)

$$\Delta I = 2g^2 \sin(2\theta_0) |\alpha^2| (\Delta\theta_b - \Delta\theta_a) \propto \beta_a \cos(\Omega_L^a t) - \beta_b \cos(\Omega_L^b t) \quad (5)$$

where $\Delta\theta_b - \Delta\theta_a$ contains the amplitude of the magnetic field gradient. To obtain the magnetic field gradient, we demodulate optical rotation signal ΔI with modulation frequency Ω_m and obtain the quadrature component of the magnetic resonance Y (48)

$$Y = Y_a - Y_b = \frac{A_a \omega_a (\Omega_L^a - \Omega_m)}{\omega_a^2 + (\Omega_L^a - \Omega_m)^2} - \frac{A_b \omega_b (\Omega_L^b - \Omega_m)}{\omega_b^2 + (\Omega_L^b - \Omega_m)^2} \quad (6)$$

where Y_a and $-Y_b$ are the magnetic resonances from S_a and S_b , respectively, with amplitude $A_{a,b} \propto \beta_{a,b}$ and linewidth $\omega_{a,b} \propto 1/\tau_{a,b}$. τ_a and τ_b are the coherence times for the two atomic sensors. Because we measure the difference between $\Delta\theta_a$ and $\Delta\theta_b$, there is a direct π phase shift between the magnetic resonances from the two sensors as shown in Eq. 6. To operate the gradiometer, we measure the magnetic resonance Y by scanning the detuning Δ_m between Ω_L and Ω_m so as to find the optimal Ω_m , where Y is sensitive to the magnetic field gradient and insensitive to the common-mode magnetic (CMM) field. For $\Omega_L^a = \Omega_L^b = \Omega_m$, the response of gradiometer to the change of magnetic field is

$$\delta Y = \frac{\delta Y_a}{\partial \Omega_L^a} \delta \Omega_L^a - \frac{\delta Y_b}{\partial \Omega_L^b} \delta \Omega_L^b = (k_a - k_b) \delta \Omega_L + \frac{k_a + k_b}{2} \delta \Omega_L^g \quad (7)$$

where $k_{a,b} = \partial Y_{a,b} / \partial \Omega_L^{a,b} = A_{a,b} / \omega_{a,b}$ denote the slopes of the magnetic resonances from S_a and S_b . $\delta \Omega_L = (\partial \Omega_L^a + \partial \Omega_L^b) / 2$ denotes the CMMN, and $\delta \Omega_L^g = \delta \Omega_L^a - \delta \Omega_L^b$ denotes the gradient field signal.

The magnetic resonances with $k_a = k_b$ are plotted in Fig. 3 (A and B) as a function of the detuning $\Delta_m = \Omega_L - \Omega_m$ obtained by scanning Ω_m . The dashed lines represent the magnetic resonances Y (black dashed line), Y_a (red dashed line), and $(-Y_b)$ (blue dashed line) without any magnetic field gradient, that is, $\Omega_L^a = \Omega_L^b$. As shown in Fig. 3A, by applying a magnetic field gradient $\delta \Omega_L^g$, that is, $\delta \Omega_L^a \neq \delta \Omega_L^b$, the two magnetic resonances Y_a (red solid line) and $(-Y_b)$ (blue solid line) move in opposite directions, so that the magnetic resonance Y (black solid line) changes markedly at the $\Delta_m = 0$, exhibiting that the most sensitive point for gradient field measurement is the zero-crossing point ($\Omega_L^a = \Omega_L^b = \Omega_m$). On the other hand, as shown in Fig. 3B, by applying a small CMM field change

$\delta \Omega_L$, both the magnetic resonances Y_a and $(-Y_b)$ move in the identical direction, and then, the corresponding magnetic resonance Y is shifted in the same direction. In this case, the magnetic resonance Y does not respond to the CMM field at $\Delta_m = 0$. Thus, the zero-crossing point is also the best working point to immune CMMN. The experimental results of the magnetic resonances of gradiometer (the line with black triangles), sensor S_a (the line with red circles) and S_b (the line with blue squares) are given in Fig. 3C. Evidently, in the middle region around $\Delta_m = 0$, the magnetic resonance Y is insensitive to the CMMN.

Noise reduction

The sensitive measurement of magnetic field at low frequencies has been a great challenge for practical applications (15–17). To realize an ultrasensitive quantum gradiometer at the frequencies below kilohertz, the technologies developed above, including sensing magnetic field, squeezing quantum noise with entangled light, and reducing CMMN by gradiometric detection, are integrated to achieve as large a signal as possible, remain the CMMN minimized, and suppress quantum noise below the PSN.

Before entering atomic sensors, the intensity-difference noise of entangled twin beams \hat{a}_1 and \hat{b}_1 from FWM process is detected and given in red line in Fig. 4A. Here, the squeezing spans a frequency range from 125 kHz to 6 MHz and the maximum squeezing is 7 dB at 0.6 MHz. To find the optimal Ω_L to perform magnetic measurement, one of the two sensors is “turned off” by blocking the optical pumping and repumping of this sensor, e.g., S_b . The power spectrum of the detected optical rotation signal oscillating at Ω_L^a is plotted in Fig. 4B. The intensity-difference squeezing (IDS) of the twin beams is naturally mapped into the power spectrum and measure the magnetic field at frequency f with squeezing at frequency $\Omega_L + f$ (50). To determine the magnetic field from the detected optical rotation signal with quantum squeezing, one needs to demodulate this signal with a frequency of $\Omega_m = \Omega_L^a$. A particular $\Omega_L^a = 152$ kHz with 5.5-dB squeezing is chosen here to optimize the sensitivity of magnetic measurements by balancing the different influences from nonlinear Zeeman effect, optical noise squeezing, and the residual magnetic resonance of the $F = 1$ state (see Supplementary Text 2). Here, a magnetic field up to 2.17×10^4 nT is applied along $-\hat{x}$, and, according to $\Omega_L^a = \gamma |B|$, we can obtain the corresponding Larmor frequency is 152 kHz, where γ is the gyromagnetic ratio, $\gamma = 7$ Hz/nT. The available squeezing at $\Omega_L^a = 152$ kHz remains 5.5 dB due to the absorption losses of the two ^{87}Rb cells (11% for S_a and 7% for S_b).

To cooperate the reduction of CMMN and suppression of quantum noise simultaneously, both sensors are “turned on” by sending optical pumping and repumping beams into them. Then, \hat{a}_2 and \hat{b}_2 are modulated with the Larmor precession of the atomic spin in S_a and S_b , respectively. The optical rotation signal is demodulated and detected to give the difference between the magnetic resonances from S_a and S_b . In this work, as the probes of gradiometer, the twin beams generated from a nondegenerate FWM process have different frequencies, leading to the different linewidths and amplitudes of the two magnetic resonances. However, the slopes of the magnetic resonances still can be set to the same, $k_a = k_b$, by tuning the one-photon detuning Δ , because the frequencies of the twin beams change following the one-photon detuning.

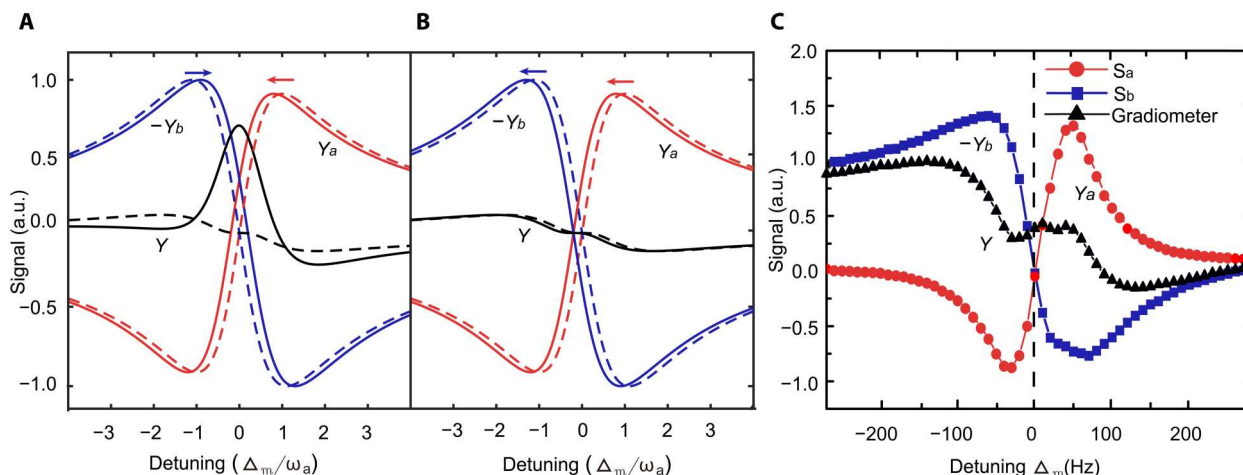


Fig. 3. Magnetic resonance of gradiometer. (A and B) Schematic diagram of the magnetic resonances with a change of magnetic field gradient (A) and common-mode magnetic (CMM) field (B). The red and blue lines represent the magnetic resonances [Y_a and $(-Y_b)$] of the two sensors, while the black line denotes the subtracted magnetic resonance (Y). When we apply a small magnetic field change, the magnetic resonances move from the dashed lines to the solid lines. (A) By applying a magnetic field gradient, the magnetic resonances (blue/red) move in the opposite direction. The subtracted magnetic resonance (black) changes obviously. (B) After applying a CMM field, both magnetic resonances (blue/red) move in the same direction. The change in the subtracted magnetic resonance (black) is inappreciable. (C) Measured magnetic resonances. The line with red circles and the line with blue squares represent the magnetic resonances of S_a with linewidth $\omega_a = 35$ Hz, and S_b with linewidth $\omega_b = 45$ Hz, which are measured by blocking optical pumping and repumping of S_a and S_b , respectively. The coherence time of S_a and S_b is 4.5 and 3.5 ms, respectively. The line with the black triangles is obtained by “turning on” both sensors simultaneously. The dashed line denotes the frequency where we measure the sensitivity. a.u., arbitrary unit.

As seen in Fig. 4C, a crossover point, where $k_a = k_b$ is achieved at $\Delta = 1.02$ GHz. This frequency is chosen for our final measurement of sensitivity. The CMRR (7, 51, 52) of the gradiometer in phase-locked loop reaches 5000 as shown in the inset of Fig. 4C, which is measured by applying a CMM field and detecting the residual of the CMM field in the difference. Meanwhile, quantum noise squeezing can still remain optimal in 5.5 dB.

Sensitivity enhancement

After noise optimization in Fig. 4, the optimal point with $\Omega_m = \Omega_L = 152$ kHz and $\Delta = 1.02$ GHz are chosen to measure the magnetic field and gradient field sensitivities of the sensors that are given in Fig. 5. The sensitivity with a single sensor S_a is shown in the blue line (a) of Fig. 5, which is limited by both CMMN and PSN. As a comparison, the red line (b) shows the sensitivity of the classical gradiometer using two coherent probe beams. Evidently, the CMMN is suppressed in this gradiometer, and the noise floor is lowered to PSN limit ~ 35 fT/cm $\sqrt{\text{Hz}}$. When the entangled twin beams replace the coherent beams as the probes of two sensors in quantum gradiometer, the sensitivity is further improved starting from 7 Hz with the help of 5.5-dB squeezing as shown in the purple line (c) of Fig. 5. The optimal sensitivity of 18 fT/cm $\sqrt{\text{Hz}}$ is achieved at 20 Hz. The sensitivity starts getting worse at both low and high frequencies due to the $1/f$ noise and the bandwidth-limited frequency response of each sensor, respectively. The frequency response of each sensor, which acts as a low-pass filter with the transfer function $b/\sqrt{f^2 + b^2}$, leads to the decrease of the signal at the increasing measurement frequency f beyond the bandwidth b and, hence, the reduction of the signal-to-noise ratio (SNR).

DISCUSSION

We construct and demonstrate a way to achieve simultaneous suppression in both PSN and CMMN by combining the techniques of quantum entanglement with gradiometric detection. With a 5.5-dB squeezed degree and a CMRR of 5000 in phase-locked loop, the sensitivity is enhanced from the subpicotesla to 10-femtotesla level. The gradient field sensitivity reaches 18 fT/cm $\sqrt{\text{Hz}}$ with a 1-cm baseline at 20 Hz, which is comparable to the sensitivity of the classical gradiometer operating with orders of magnitude more atoms. This work brings quantum enhancement of the magnetic sensitivity to the low-frequency range starting from 7 Hz. Such quantum-enhanced magnetic gradiometer is promising for practical applications where the characteristic magnetic signatures appear at low frequencies in challenging environments (53).

The scheme of the entangled sensing of the magnetic field can be extended by cascaded FWM (43) and achieve a network of entangled magnetic sensors. There are still many possibilities to improve the performance of magnetometry with the technical routes of combining the quantum manipulation and atom-light interface. The bandwidth and CMRR of magnetometry can be further improved in several ways such as operating magnetometry in self-oscillating mode (54) or observing the free induction decay of atomic spin (52). The low-frequency $1/f$ noise appears in Fig. 5 (b and c) caused by temperature shifting in the shield can be decreased by a better temperature control system. Moreover, in this work, the atom number and photon number satisfying $N_{\text{at}}^{1/2} N_{\text{ph}} < \eta^{1/2} (\Delta_p/\Gamma_0)^2 (A/\lambda^2)^{3/2}$, so that the SPN does not limit the sensitivity. For optimized magnetometry with comparable noises from atom and light, the sensitivity can still be improved with the use of correlated twin beams (see details in Materials and Methods).

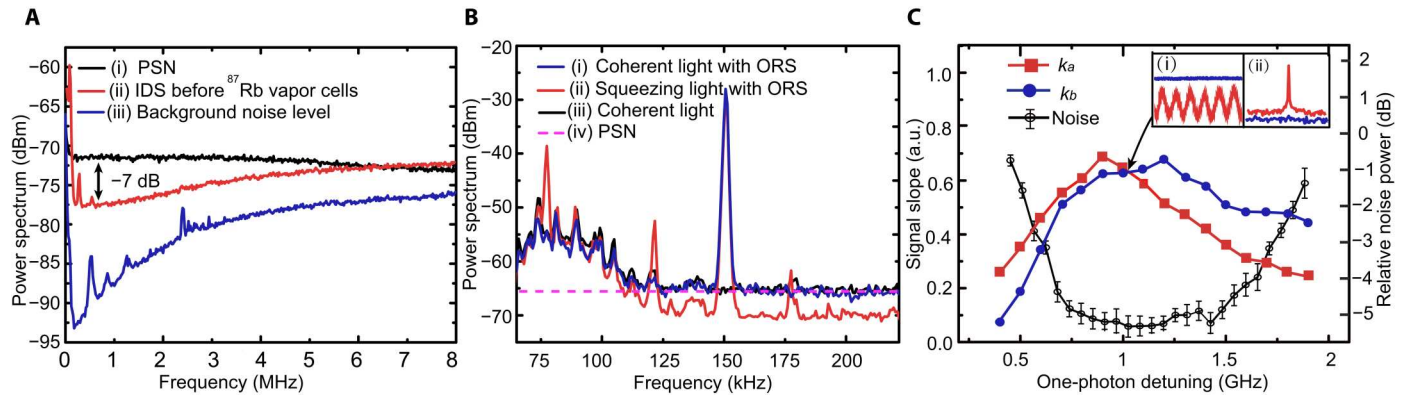


Fig. 4. Noise of entangled twin beam. (A) Noise power spectrum directly measured after the GT polarizer. The BPD's transimpedance gain is 10^5 V/A with a bandwidth of 5 MHz. The resolution bandwidth (RBW) and video bandwidth (VBW) are 30 kHz and 300 Hz, respectively. The peaks appearing at low frequencies are electronic noises. (i) The black line denotes the PSN. (ii) The red line denotes the intensity-difference squeezing (IDS) between the twin beams. (iii) The blue line denotes the background noise level. (B) Power spectrum measured after the ^{87}Rb cells. To measure the optical rotation signal (ORS) at 152 kHz and avoid electronic noise, the BPD transimpedance gain is 10^6 V/A with a bandwidth of 300 kHz. (i and ii) The blue and red lines denote the noise power spectrum measured by coherent light and squeezed light with an optical rotation signal at 152 kHz from S_a . (iii) The black line denotes the noise power spectrum measured by coherent light. Here, the noise at low frequencies is dominated by laser excess noise. (iv) The purple dash line represents PSN. RBW, 1 kHz; VBW, 300 Hz. (C) The slopes of the magnetic resonances of S_a (the line with red squares, left vertical scale) and S_b (the line with solid blue circles, left vertical scale) and the noise power relative to PSN (the line with hollow black circles, right vertical scale) change with one-photon detuning. Inset: (i) The measured magnetic signal and (ii) their Fourier transform of S_a (red line) and gradiometer (blue line).

MATERIALS AND METHODS

Phase-insensitive amplifier

Using the relations of the two-mode squeezed state (Eqs. 1 and 2) with coherent input $|\alpha\rangle$ ($\alpha = |\alpha|e^{i\Phi_a}$) at mode \hat{a}_{in} and vacuum input at mode \hat{b}_{in} , we can obtain the noise in the difference between the mean numbers of photons

$$\text{Var}(\hat{a}_1^\dagger \hat{a}_1 - \hat{b}_1^\dagger \hat{b}_1) = |\alpha|^2 \quad (8)$$

To obtain the level of squeezing, we take the difference noise of coherent light with the same intensities ($|\alpha|^2$ and 0) as the coherent state

$$\begin{aligned} \text{Var}(\hat{a}_1^\dagger \hat{a}_1 - \hat{b}_1^\dagger \hat{b}_1)_{\text{SNL}} \\ = \langle \hat{a}_1^\dagger \hat{a}_1 \rangle + \langle \hat{b}_1^\dagger \hat{b}_1 \rangle \\ = |\alpha|^2 (G^2 + g^2) + 2g^2 \end{aligned} \quad (9)$$

where the subscript SNL represents the shot noise limit, $G^2 - g^2 = 1$, and we defined the R_{ab} as the ratio between these two fluctuations as

$$\begin{aligned} R_{ab} &= \frac{\text{Var}(\hat{a}_1^\dagger \hat{a}_1 - \hat{b}_1^\dagger \hat{b}_1)}{\text{Var}(\hat{a}_1^\dagger \hat{a}_1 - \hat{b}_1^\dagger \hat{b}_1)_{\text{SNL}}} \\ &= \frac{|\alpha|^2}{|\alpha|^2(G^2 + g^2) + 2g^2} \end{aligned} \quad (10)$$

Here, $|\alpha|^2 \gg 1$ and $|\alpha| \gg g$, and we have

$$R_{ab} = \frac{1}{G^2 + g^2} = \frac{1}{2G^2 - 1} \quad (11)$$

As we can see, the level of squeezing increases with the gain G and is independent of phases Φ_p and Φ_a . Hence, the parametric

amplifier (PA) process with vacuum input at one of the port can be regarded as a phase-insensitive amplifier.

Detail for the theory

We generate intensity correlated two-mode squeezed fields by PA process in hot ^{85}Rb vapor. By mixing and amplifying the two field modes \hat{a}_{in} and \hat{b}_{in} , correlations between two modes are

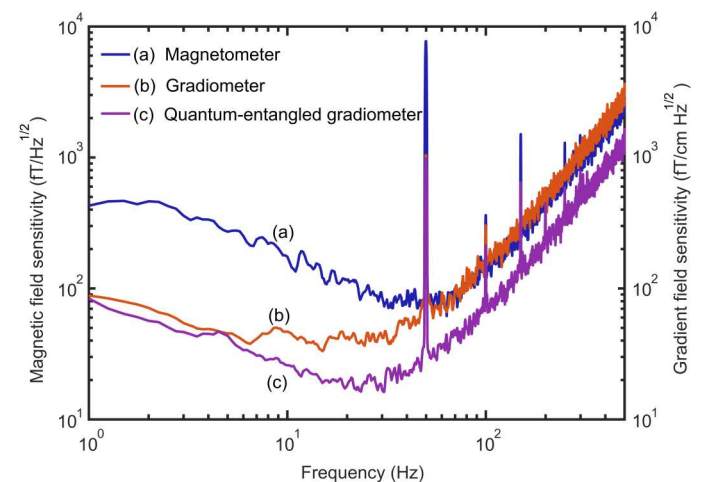


Fig. 5. Magnetic field and gradient field sensitivities. The transfer function of the low-pass filter (3, 57) is $b/\sqrt{f^2 + b^2}$, where the bandwidth $b = (\omega_a + \omega_b)/2 = 40$ Hz. (a) Sensitivity of the magnetometer limited by PSN and CMMN. (b) Gradient field sensitivity of the gradiometer limited by PSN. (c) Gradient field sensitivity of the gradiometer with 5.5-dB squeezing.

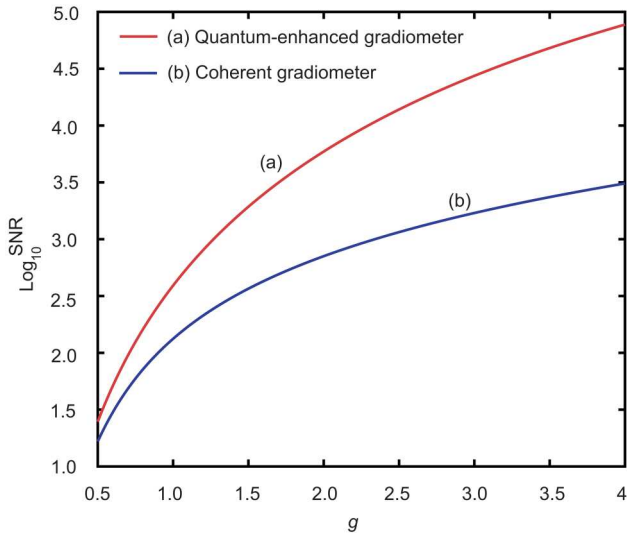


Fig. 6. The improvement of SNR changes with g . (a) Quantum-enhanced gradiometer and (b) coherent gradiometer. Here, we set $\alpha = 100$, $\theta_0 = 0.05$, and $(\Delta\theta_b - \Delta\theta_a)^2 = 1$.

generated (55)

$$\begin{bmatrix} \hat{a}_x \\ \hat{a}_x^\dagger \\ \hat{b}_x \\ \hat{b}_x^\dagger \end{bmatrix} = \begin{bmatrix} G & 0 & 0 & e^{-i\Phi_p} g \\ 0 & G & e^{i\Phi_p} g & 0 \\ 0 & e^{i\Phi_p} g & G & 0 \\ e^{-i\Phi_p} g & 0 & 0 & G \end{bmatrix} \begin{bmatrix} \hat{a}_{in} \\ \hat{a}_{in}^\dagger \\ \hat{b}_{in} \\ \hat{b}_{in}^\dagger \end{bmatrix} \quad (12)$$

In our system, with a coherent state $|\alpha\rangle$ input at port \hat{a}_{in} and a vacuum state at port \hat{b}_{in} , \hat{a}_x and \hat{b}_x are the outputs of the PA process. Both of the fields are linearly polarized along the x direction.

\hat{a}_x and \hat{b}_x act as the probe beams of two ^{87}Rb vapor sensors \hat{a}_1 and \hat{b}_1 and couple the magnetic field into their polarizations. The polarizations of \hat{a}_2 and \hat{b}_2 are rotated with angles $\Delta\theta_a$ and $\Delta\theta_b$, \hat{a}_2 and \hat{b}_2 are further rotated by a HWP with angle θ_0 and mixed with a vacuum state with y polarization \hat{a}_y^{in} and \hat{b}_y^{in} at the PBS, respectively. The output of the PBS is

$$\begin{bmatrix} \hat{a}_x^{out} \\ \hat{a}_y^{out} \\ \hat{b}_x^{out} \\ \hat{b}_y^{out} \end{bmatrix} = \begin{bmatrix} \cos(\theta_a) & -\sin(\theta_a) & 0 & 0 \\ \sin(\theta_a) & \cos(\theta_a) & 0 & 0 \\ 0 & 0 & \cos(\theta_b) & -\sin(\theta_b) \\ 0 & 0 & \sin(\theta_b) & \cos(\theta_b) \end{bmatrix} \times \begin{bmatrix} \hat{a}_x \\ \hat{a}_y^{in} \\ \hat{b}_x \\ \hat{b}_y^{in} \end{bmatrix} \quad (13)$$

where $\theta_a = \theta_0 + \Delta\theta_a$, $\theta_b = \theta_0 + \Delta\theta_b$. The input-output relation of

optical field after the whole process is

$$\begin{bmatrix} \hat{a}_x^{out} \\ \hat{a}_y^{out} \\ \hat{b}_x^{out} \\ \hat{b}_y^{out} \end{bmatrix} = \begin{bmatrix} G\cos(\theta_a) & 0 & 0 & e^{i\Phi_p} g\cos(\theta_a) & -\sin(\theta_a) & 0 & 0 & 0 \\ 0 & G\cos(\theta_a) & e^{-i\Phi_p} g\cos(\theta_a) & 0 & 0 & -\sin(\theta_a) & 0 & 0 \\ G\sin(\theta_a) & 0 & 0 & e^{i\Phi_p} g\sin(\theta_a) & \cos(\theta_a) & 0 & 0 & 0 \\ 0 & G\sin(\theta_a) & e^{-i\Phi_p} g\sin(\theta_a) & 0 & 0 & \cos(\theta_a) & 0 & 0 \\ 0 & e^{i\Phi_p} g\cos(\theta_b) & G\cos(\theta_b) & 0 & 0 & 0 & -\sin(\theta_b) & 0 \\ e^{-i\Phi_p} g\cos(\theta_b) & 0 & 0 & G\cos(\theta_b) & 0 & 0 & 0 & -\sin(\theta_b) \\ 0 & e^{i\Phi_p} g\sin(\theta_b) & G\sin(\theta_b) & 0 & 0 & 0 & \cos(\theta_b) & 0 \\ e^{-i\Phi_p} g\sin(\theta_b) & 0 & 0 & G\sin(\theta_b) & 0 & 0 & 0 & \cos(\theta_b) \end{bmatrix} \times \begin{bmatrix} \hat{a}_{in} \\ \hat{a}_{in}^\dagger \\ \hat{b}_{in} \\ \hat{b}_{in}^\dagger \\ \hat{a}_y^{in} \\ \hat{a}_y^{in\dagger} \\ \hat{b}_y^{in} \\ \hat{b}_y^{in\dagger} \end{bmatrix} \quad (14)$$

The output fields of PBS are sent to the balanced photodetector and achieve the intensity-difference measurement. The observation of magnetometer is

$$\hat{I} = \hat{I}_x^a - \hat{I}_y^a - \hat{I}_x^b + \hat{I}_y^b \quad (15)$$

where $\hat{I}_x^a = \hat{a}_x^{out\dagger} \hat{a}_x^{out}$, $\hat{I}_y^a = \hat{a}_y^{out\dagger} \hat{a}_y^{out}$, $\hat{I}_x^b = \hat{b}_x^{out\dagger} \hat{b}_x^{out}$, $\hat{I}_y^b = \hat{b}_y^{out\dagger} \hat{b}_y^{out}$. The average value of \hat{I} is

$$\langle \hat{I} \rangle = [G^2 \cos(2\theta_a) - g^2 \cos(2\theta_b)] |\alpha|^2 + g^2 [\cos(2\theta_a) - \cos(2\theta_b)] \quad (16)$$

When operate at $\theta_a = \theta_b = 0$, the fluctuation of magnetometer is

$$\text{Var}(\hat{I}) = [1 + g^2 - g^2 \cos(4\theta_0)] |\alpha|^2 + 2\sin^2(2\theta_0) g^2 \quad (17)$$

The change in the observation of magnetometer with perturbation $\Delta\theta_a$ and $\Delta\theta_b$ is

$$\begin{aligned} \Delta I &= \frac{\partial \langle \hat{I} \rangle}{\partial \theta_a} \Delta\theta_a + \frac{\partial \langle \hat{I} \rangle}{\partial \theta_b} \Delta\theta_b \\ &= 2[g^2 \sin(2\theta_b) \Delta\theta_b - G^2 \sin(2\theta_a) \Delta\theta_a] |\alpha|^2 \\ &\quad + 2g^2 [\sin(2\theta_b) \Delta\theta_b - \sin(2\theta_a) \Delta\theta_a] \end{aligned} \quad (18)$$

For $\Delta\theta_a \ll \theta_a$, $\Delta\theta_b \ll \theta_b$, $|\alpha|^2 \gg 1$ and $G \approx g \gg 1$, we have

$$\Delta I = 2g^2 \sin(2\theta_0) |\alpha|^2 (\Delta\theta_b - \Delta\theta_a) \quad (19)$$

Hence, the SNR is

$$\frac{(\Delta I)^2}{\text{Var}(\hat{I})} = \frac{4g^4 \sin^2(2\theta_0) |\alpha|^4 (\Delta\theta_b - \Delta\theta_a)^2}{[1 + g^2 - g^2 \cos(4\theta_0)] |\alpha|^2 + 2\sin^2(2\theta_0) g^2} \quad (20)$$

The SNRs of the gradiometer change with g are plotted in Fig. 6. The red line and the blue line represent the SNR of quantum-enhanced gradiometer and coherent gradiometer, respectively. We can see that, with the increase of g , the SNR of the squeezed gradiometer is always better than the coherent gradiometer.

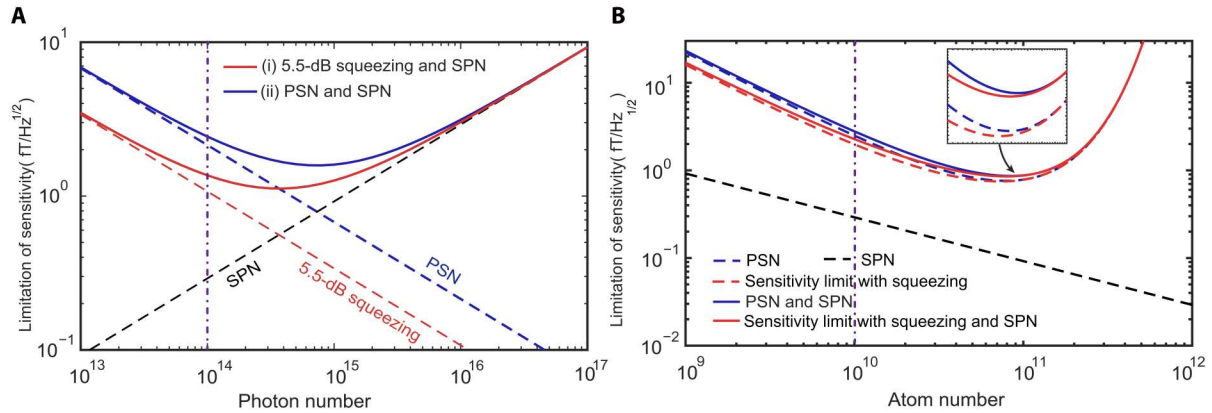


Fig. 7. The overall sensitivity limitations. (A) Sensitivity change with N_{ph} and (B) sensitivity change with N_{at} . Here, we choose $\gamma = 7 \text{ Hz/nT}$, $\tau_m = 1 \text{ s}$, $\Delta_p = 8 \text{ GHz}$, $\Gamma_0 = 5.7 \text{ MHz}$, $A = 6 \times 10^{-4} \text{ m}^2$, $\lambda = 795 \text{ nm}$, which are consistent with the experimental condition. The atom number in (A) is $N_{at} = 10^{10}$ and photon number in (B) is $N_{ph} = 10^{14}$. The purple dash-dot lines are the number of photons and atoms in the experiment.

Fundamental limitation of sensitivity

For magnetometry based on optical readout of atomic ensemble's spin precession, the sensitivity is fundamentally limited PSN and SPN. The corresponding sensitivity δB_{ph} and δB_{at} can be described as (30)

$$\delta B_{ph} = \frac{1}{\gamma \tau_m} \frac{1}{N_{at} \sqrt{\eta N_{ph}}} \frac{\Delta_p A}{\Gamma_0 \lambda^2} \quad (21)$$

$$\delta B_{at} = \frac{1}{\gamma \tau_m} \frac{\sqrt{N_{ph}} \Gamma_0}{\sqrt{N_{at}} \Delta_p} \left(\frac{\lambda^2}{A} \right)^{1/2} \quad (22)$$

where γ is the gyromagnetic ratio and τ_m is the measurement time. $\eta = \exp[-N_{at} \Gamma_0^2 \sigma / (\Gamma_0^2 + \Delta_p^2) A]$ is the transmittance of the probe field that has positive relation with the atom number. N_{at} and N_{ph} are the total number of atoms and input photons used in the measurement, respectively. Γ_0 is the natural transition width, Δ_p is the frequency detuning from optical resonance, and λ is the light wavelength. A is the cross section of the probe and assumed to match the atomic sample, and σ is the photon absorption cross section that only depends on the wavelength of the transition (48). Considering the noise from both atom and light, the sensitivity is limited by the larger one of δB_{at} and δB_{ph} . When the atom number and photon number satisfying $N_{at}^{1/2} N_{ph} < \eta^{1/2} (\Delta_p / \Gamma_0)^{1/2} (A / \lambda^2)^{3/2}$, we get $\delta B_{ph} > \delta B_{at}$. The sensitivity is limited by PSN. In our work, N_{at} is limited by the operation temperature of vapor cell, and N_{ph} is limited by the FWM process. In consequence, the sensitivity of gradiometer with coherent light is fundamentally limited by PSN. With the use of a squeezed light, the sensitivity can further break PSN.

The overall sensitivity limitations with the change of N_{ph} and N_{at} are plotted in Fig. 7. We can find the optimum number of photons, atoms, and corresponding sensitivity by minimizing the overall uncertainty with coherent light and squeezed light. In Fig. 7B, the higher atom number leads to higher probe absorption, which limits the amount of detected photon number and optical squeezing. Compared with coherent light, the use of squeezed light can lead to a better sensitivity with lower number of photons or atoms.

In (30), the sensitivity is discussed in free induction decay scheme. When the number of spins that flip due to ground-state relaxation becomes comparable to unity, uncertainty due to

relaxation begins to dominate the atomic noise. There is no improvement in sensitivity with squeezed light. While, in our work, the decayed spin is repolarized by synchronized pumping. With long measurement time, the sensitivity still can be improved by the squeezed light.

Experimental layout

The cell (12.5 mm long) generating FWM process contains isotopically pure ^{85}Rb vapor that can be heated to over 120°C . It is antireflection (AR)-coated on all four surfaces to achieve a high transmission efficiency ($\sim 95\%$). Both FWM pump and seed are focused in the center of the cell with beam waists of 500 and 250 μm , respectively.

The sensors (S_a and S_b) of the gradiometer are mainly constructed by two paraffin-coated, AR-coated cylindrical, and isotopically enriched ^{87}Rb vapor cells (56) (1 cm in length and 1 cm in diameter) that are placed side by side in a three-layer μ -metal magnetic shield. The two cells are heated to 35°C for sensitivity optimization. To generate CMM field and magnetic field gradient on two sensors, we add a set of Helmholtz coil and a set of anti-Helmholtz coil with a diameter of 92 mm outside of two ^{87}Rb vapor cells.

When measuring the squeeze degree, the PSN is calibrated by coherent light with same power of squeezed light. To realize the coherent gradiometer and ensure the same experimental conditions, the probes of coherent gradiometer are also generated by FWM process. We change the temperature of the ^{85}Rb vapor cell to 100°C to tune the gain factor of the FWM process so that the noise spectrum of the IDS in this case is consistent with that of the coherent light. The laser power of each channel is detected by monitor of BPD and is sent to the oscilloscope. We calibrate the power of the laser on the oscilloscope so that the laser power is same in the two measurements.

Supplementary Materials

This PDF file includes:

Supplementary Text
Figs. S1 to S4
References

REFERENCES AND NOTES

- D. Budker, W. Gawlik, D. F. Kimball, S. M. Rochester, V. V. Yashchuk, A. Weis, Resonant nonlinear magneto-optical effects in atoms. *Rev. Mod. Phys.* **74**, 1153–1201 (2002).
- I. K. Kominis, T. W. Kornack, J. C. Allred, M. V. Romalis, A subfemtotesla multichannel atomic magnetometer. *Nature* **422**, 596–599 (2003).
- D. Budker, M. Romalis, Optical magnetometry. *Nat. Phys.* **3**, 227–234 (2007).
- M. P. Ledbetter, I. M. Savukov, V. M. Acosta, D. Budker, M. V. Romalis, Spin-exchange-relaxation-free magnetometry with Cs vapor. *Phys. Rev. A* **77**, 033408 (2008).
- H. B. Dang, A. C. Maloof, M. V. Romalis, Ultrahigh sensitivity magnetic field and magnetization measurements with an atomic magnetometer. *Appl. Phys. Lett.* **97**, 151110 (2010).
- D. Sheng, S. Li, N. Dural, M. V. Romalis, Subfemtotesla scalar atomic magnetometry using multipass cells. *Phys. Rev. Lett.* **110**, 160802 (2013).
- D. Sheng, A. R. Perry, S. P. Krzyzewski, S. Geller, J. Kitching, S. Knappe, A microfabricated optically-pumped magnetic gradiometer. *Appl. Phys. Lett.* **110**, 031106 (2017).
- S. K. Lee, K. L. Sauer, S. J. Seltzer, O. Alem, M. V. Romalis, Subfemtotesla radio-frequency atomic magnetometer for detection of nuclear quadrupole resonance. *Appl. Phys. Lett.* **89**, 214106 (2006).
- S. Groeger, G. Bison, P. E. Knowles, R. Wynands, A. Weis, Laser-pumped cesium magnetometers for high-resolution medical and fundamental research. *Sens. Actuator A Phys.* **129**, 1–5 (2006).
- G. Vasilakis, J. M. Brown, T. W. Kornack, M. V. Romalis, Limits on new long range nuclear spin-dependent forces set with a $K^3\text{He}$ comagnetometer. *Phys. Rev. Lett.* **103**, 261801 (2009).
- I. Altarev, C. A. Baker, G. Ban, G. Bison, K. Bodek, M. Daum, P. Fierlinger, P. Geltenbort, K. Green, M. G. D. van der Grinten, E. Gutsmedl, P. G. Harris, W. Heil, R. Henneck, M. Horras, P. Iaydjiev, S. N. Ivanov, N. Khomutov, K. Kirch, S. Kistryn, A. Knecht, P. Knowles, A. Kozela, F. Kuchler, M. Kuźniak, T. Lauer, B. Lauss, T. Lefort, A. Mtchedlishvili, O. Naviliat-Cuncic, A. Pazgalev, J. M. Pendlebury, G. Petzoldt, E. Pierre, G. Pignol, G. Quemener, M. Rebetez, D. Rebreyend, S. Roccia, G. Rogel, N. Severijns, D. Shiers, Y. Sobolev, A. Weis, J. Zejma, G. Zsigmond, Test of Lorentz invariance with spin precession of ultracold neutrons. *Phys. Rev. Lett.* **103**, 081602 (2009).
- M. S. Safronova, D. Budker, D. DeMille, D. F. J. Kimball, A. Derevianko, C. W. Clark, Search for new physics with atoms and molecules. *Rev. Mod. Phys.* **90**, 025008 (2018).
- M. Jiang, H. Su, A. Garcon, X. Peng, D. Budker, Search for axion-like dark matter with spin-based amplifiers. *Nat. Phys.* **17**, 1402–1407 (2021).
- I. M. Savukov, V. S. Zotev, P. L. Volegov, M. A. Espy, A. N. Matlashov, J. J. Gomez, R. H. Kraus Jr., MRI with an atomic magnetometer suitable for practical imaging applications. *J. Magn. Reson.* **199**, 188–191 (2009).
- E. Boto, N. Holmes, J. Leggett, G. Roberts, V. Shah, S. S. Meyer, L. D. Muneyner, L. D. Muñoz, K. J. Mullinger, T. M. Tierney, S. Bestmann, G. R. Barnes, R. Bowtell, M. J. Brookes, Moving magnetoencephalography towards real-world applications with a wearable system. *Nature* **555**, 657–661 (2018).
- R. M. Hill, E. Boto, N. Holmes, C. Hartley, Z. A. Seadat, J. Leggett, G. Roberts, V. Shah, T. M. Tierney, M. W. Woolrich, C. J. Stagg, G. R. Barnes, R. Bowtell, R. Slater, M. J. Brookes, A tool for functional brain imaging with lifespan compliance. *Nat. Commun.* **10**, 1–11 (2019).
- K. Jensen, M. A. Skarsfeldt, H. Stærkind, J. Arnbak, M. V. Balabas, S.-P. Olesen, B. H. Bentzen, E. S. Polzik, Magnetocardiography on an isolated animal heart with a room-temperature optically pumped magnetometer. *Sci. Rep.* **8**, 1–9 (2019).
- K. Zhu, A. M. Shah, J. Berkow, Miniature coil array for passive magnetocardiography in non-shielded environments. *IEEE J. Electromagn. RF and Microw. Med. Biol.* **5**, 124–131 (2020).
- E. Elzenheimer, H. Laufs, Magnetic measurement of electrically evoked muscle responses with optically pumped magnetometers. *IEEE Trans. Neur. Sys. Reh.* **28**, 756–765 (2020).
- T. Theis, P. Ganssle, G. Kervern, S. Knappe, J. Kitching, M. P. Ledbetter, D. Budker, A. Pines, Parahydrogen-enhanced zero-field nuclear magnetic resonance. *Nat. Phys.* **7**, 571–575 (2011).
- J. W. Blanchard, D. Budker, A. Trabesinger, Lower than low: Perspectives on zero- to ultralow-field nuclear magnetic resonance. *J. Magn. Reson.* **323**, 106886 (2021).
- Y. J. Kim, I. Savukov, J. H. Huang, P. Nath, Magnetic microscopic imaging with an optically pumped magnetometer and flux guides. *Appl. Phys. Lett.* **110**, 043702 (2017).
- C. Deans, L. Marmugi, S. Hussain, F. Renzoni, Electromagnetic induction imaging with a radio-frequency atomic magnetometer. *Appl. Phys. Lett.* **108**, 103503 (2016).
- C. Deans, L. Marmugi, F. Renzoni, Through-barrier electromagnetic imaging with an atomic magnetometer. *Opt. Express* **25**, 17911–17917 (2017).
- M. C. D. Tayler, J. Ward-Williams, L. F. Gladden, Ultralow-field nuclear magnetic resonance of liquids confined in ferromagnetic and paramagnetic materials. *Appl. Phys. Lett.* **115**, 072409 (2019).
- Y. Hu, G. Z. Iwata, M. Mohammadi, E. V. Silleta, A. Wickenbrock, J. W. Blanchard, D. Budker, A. Jerschow, Sensitive magnetometry reveals inhomogeneities in charge storage and weak transient internal currents in Li-ion cells. *Proc. Natl. Acad. Sci. U.S.A.* **117**, 10667–10672 (2020).
- F. P. Bustos, D. B. Callia, D. Budker, M. Centrone, J. Hellemeier, P. Hickson, R. Holzlohner, S. Rochester, Remote sensing of geomagnetic fields and atomic collisions in the mesosphere. *Nat. Commun.* **9**, 1–8 (2018).
- M. H. Acuna, Space-based magnetometers. *Rev. Sci. Instrum.* **73**, 3717–3736 (2002).
- B. Lawrie, P. Raphael, P. Maksymovych, Squeezing noise in microscopy with quantum light. *Trends Chem.* **2**, 683–686 (2020).
- M. Auzinsh, D. Budker, D. F. Kimball, S. M. Rochester, J. E. Stalnaker, A. O. Sushkov, V. V. Yashchuk, Can a quantum nondemolition measurement improve the sensitivity of an atomic magnetometer? *Phys. Rev. Lett.* **93**, 173002 (2004).
- F. Wolfgramm, A. Cerè, F. A. Beduini, A. Predojević, M. Koschorreck, M. W. Mitchell, Squeezed-light optical magnetometry. *Phys. Rev. Lett.* **105**, 053601 (2010).
- T. Horrom, R. Singh, J. P. Dowling, E. E. Mikhailov, Quantum-enhanced magnetometer with low-frequency squeezing. *Phys. Rev. A* **86**, 023803 (2012).
- N. Otterstrom, R. C. Pooser, B. J. Lawrie, Nonlinear optical magnetometry with accessible in situ optical squeezing. *Opt. Lett.* **39**, 6533–6536 (2014).
- G. Bao, S. Wu, S. Liu, W. Huang, Z. Li, L. Q. Chen, C. H. Yuan, W. Zhang, Enhancement of the signal-to-noise ratio of an atomic magnetometer by 10 dB. *Phys. Rev. Applied.* **11**, 054075 (2019).
- L. Bai, X. Wen, Y. Yang, L. Zhang, J. He, Y. Wang, J. Wang, Quantum-enhanced rubidium atomic magnetometer based on Faraday rotation via 795 nm Stokes operator squeezed light. *J. Opt.* **23**, 085202 (2021).
- C. Troullinou, R. Jiménez-Martínez, J. Kong, V. G. Lucivero, M. W. Mitchell, Squeezed-light enhancement and backaction evasion in a high sensitivity optically pumped magnetometer. *Phys. Rev. Lett.* **127**, 193601 (2021).
- J. Li, I. Novikova, Improving sensitivity of an amplitude-modulated magneto-optical atomic magnetometer using squeezed light. *JOSA. B* **39**, 2998–3003 (2022).
- K. Kamada, Y. Ito, S. Ichihara, N. Mizutani, T. Kobayashi, Noise reduction and signal-to-noise ratio improvement of atomic magnetometers with optical gradiometer configurations. *Opt. Express* **23**, 6976–6987 (2015).
- M. Jiang, R. P. Frutos, T. Wu, J. W. Blanchard, X. Peng, D. Budker, Magnetic gradiometer for the detection of zero- to ultralow-field nuclear magnetic resonance. *Phys. Rev. Appl.* **11**, 024005 (2019).
- V. G. Lucivero, W. Lee, N. Dural, Femtotesla direct magnetic gradiometer using a single multipass cell. *Phys. Rev. Appl.* **15**, 014004 (2021).
- C. F. McCormick, V. Boyer, E. Arimondo, P. D. Lett, Strong relative intensity squeezing by four-wave mixing in rubidium vapor. *Opt. Lett.* **32**, 178–180 (2007).
- V. Boyer, A. M. Marino, R. C. Pooser, P. D. Lett, Entangled images from four-wave mixing. *Science* **321**, 544–547 (2008).
- Z. Qin, L. Cao, H. Wang, A. M. Marino, W. Zhang, J. Jing, Experimental generation of multiple quantum correlated beams from hot rubidium vapor. *Phys. Rev. Lett.* **113**, 023602 (2014).
- G. K. Gulati, B. Srivathsan, B. Chng, A. Cerè, C. Kurtsiefer, Polarization entanglement and quantum beats of photon pairs from four-wave mixing in a cold ^{87}Rb ensemble. *New J. Phys.* **17**, 093034 (2015).
- R. Han, M. Balabas, C. Hovde, W. Li, H. M. Roig, T. Wang, A. Wickenbrock, E. Zhivun, Z. You, D. Budker, Is light narrowing possible with dense-vapor paraffin coated cells for atomic magnetometers? *AIP Adv.* **7**, 125224 (2017).
- Z. Y. Jiang, X. C. Liu, P. W. Lin, J. F. Qu, H. P. Liu, Enhanced fully optically pumped magnetic resonance with optical sideband auxiliary pumping. *Opt. Lett.* **45**, 105–108 (2020).
- W. E. Bell, A. L. Bloom, Optical detection of magnetic resonance in alkali metal vapor. *Phys. Rev.* **107**, 1559–1565 (1957).
- M. Auzinsh, D. Budker, S. Rochester, *Optically Polarized Atoms: Understanding Light-Atom Interactions* (Oxford University, 2010).
- S. R. de Echaniz, M. Koschorreck, M. Napolitano, M. Kubasik, M. W. Mitchell, Hamiltonian design in atomlight interactions with rubidium ensembles: A quantum-information toolbox. *Phys. Rev. A* **77**, 032316 (2008).
- F. Liu, S. Xiao, D. Wei, Y. Zhang, X. Jia, M. Xiao, Squeezing-enhanced fiber Mach-Zehnder interferometer for low-frequency phase measurement. *Appl. Phys. Lett.* **110**, 021106 (2017).
- M. E. Limes, E. L. Foley, T. W. Kornack, S. Caliga, S. McBride, A. Braun, W. Lee, V. G. Lucivero, M. V. Romalis, Portable magnetometry for detection of biomagnetism in ambient environments. *Phys. Rev. Appl.* **14**, 011002 (2020).
- V. G. Lucivero, W. Lee, M. E. Limes, E. L. Foley, T. W. Kornack, M. V. Romalis, Femtotesla nearly quantum-noiselimited pulsed gradiometer at Earth-scale fields. *Phys. Rev. Appl.* **18**, L021001 (2022).
- K.-M.C. Fu, G.Z. Iwata, A. Wickenbrock, D. Budker, Sensitive magnetometry in challenging environments. *AVS Quantum Sci.* **2**, 044702 (2020).

54. J.M Higbie, E. Corsini, D. Budker, Robust, high-speed, all-optical atomic magnetometer. *Rev.Sci.Instrum.* **77**, 113106 (2006).
55. F. Hudelist, J. Kong, C. Liu, J. Jing, Z.Y. Ou, W. Zhang, Quantum metrology with parametric amplifier-based photon correlation interferometers. *Nat. Commun.* **5**, 1–6 (2014).
56. M.V. Balabas, T. Karaulanov, M.P. Ledbetter, D. Budker, Polarized alkali-metal vapor with minute-long transverse spin-relaxation time. *Phys. Rev. Lett.* **105**, 070801 (2010).
57. V. Shah, G. Vasilakis, M.V. Romalis, High bandwidth atomic magnetometry with continuous quantum nondemolition measurements. *Phys. Rev. Lett.* **104**, 013601 (2010).
58. G. Bao, A. Wickenbrock, S. Rochester, W. Zhang, D. Budker, Suppression of the nonlinear Zeeman effect and heading error in Earth-field-range alkali-vapor magnetometers. *Phys. Rev. Lett.* **120**, 033202 (2018).
59. Z. Wang, X. Peng, R. Zhang, H. Luo, J. Li, Z. Xiong, S. Wang, H. Guo, Single-species atomic magnetometer based on ^{87}Rb atoms. *Phys. Rev. Lett.* **124**, 193002 (2020).

Acknowledgments: We thank D. Budker from Johannes Gutenberg University and D. Sheng from University of Science and Technology of China for useful discussions. **Funding:** This work was supported by the Innovation Program for Quantum Science and Technology (2021ZD0303200), the National Natural Science Foundation of China (grant nos. 12234014, 12274132, 11904227, 12204304, 91536114, 11874152, and 11654005), the Shanghai Municipal Science and Technology Major Project (grant no. 2019SHZDZX01), the Fellowship of China Postdoctoral Science Foundation (grant nos. 2020TQ0193, 2021 M702146, 2021 M702150, 2021

M702147, and 2022 T150413), the Sailing Program of the Science and Technology Commission of Shanghai Municipality (19YF1421800), Innovation Program of Shanghai Municipal Education Commission (no. 202101070008E00099), the National Key Research and Development Program of China (grant no. 2016YFA0302001), and the Fundamental Research Funds for the Central Universities. W.Z. acknowledges additional support from the Shanghai Talent Program. **Author contributions:** W.Z. supervised the whole project. G.B. and W.Z. conceived the research. G.B., L.C., and W.Z. designed the experiments. G.B., S.W., J.G., J.C., W.D., P.Y., and L.C. performed the experiment. G.B., S.W., W.D., M.S., and W.Z. contributed to the theoretical study. G.B. and S.W. analyzed the data. G.B., S.W., and J.C. draw the diagrams. G.B., S.W., L.C., and W.Z. wrote the paper. All authors contributed to the discussion and review of the manuscript. **Competing interests:** G.B., S.W., J.G., W.D., P.Y., L.C., and W.Z. are inventors on a patent related to this work filed by Shanghai Jiao Tong University (no. CN 114062981 B, published 4 November 2021). The authors declare that they have no other competing interests. **Data and materials availability:** All data needed to evaluate the conclusions in the paper are present in the paper and/or the Supplementary Materials.

Submitted 7 December 2022

Accepted 10 March 2023

Published 12 April 2023

10.1126/sciadv.adg1760